Energy and AI 20 (2025) 100478

Contents lists available at ScienceDirect

Energy and AI

journal homepage: www.elsevier.com/locate/egyai

Data-driven modeling of open circuit voltage hysteresis for $LiFePO_4$ batteries with conditional generative adversarial network

Lisen Yan [a,d,e], Jun Peng [b], Zeyu Zhu [a], Heng Li [b,*], Zhiwu Huang [c], Dirk Uwe Sauer [d,e], Weihan Li [d,e,*]

[a] School of Computer Science and Engineering, Central South University, Changsha, 410083, China
[b] School of Electronic Information, Central South University, Changsha, 410083, China
[c] School of Automation, Central South University, Changsha, 410083, China
[d] Center for Ageing, Reliability and Lifetime Prediction of Electrochemical and Power Electronics Systems (CARL), RWTH Aachen University, Campus-Boulevard 89, Aachen, 52074, Germany
[e] Institute for Power Electronics and Electrical Drives (ISEA), RWTH Aachen University, Campus-Boulevard 89, Aachen, 52074, Germany

HIGHLIGHTS

- A data-driven modeling approach to estimate the open circuit voltage of LFP cells.
- Utilizing adversarial machine learning to effectively capture hysteresis dependencies.
- Conditional matrix of temperature, SOC path and aging enhances model adaptability.
- Comprehensive hysteresis data was collected under various conditions.
- Modeling results are compared with three state-of-the-art hysteresis models.

GRAPHICAL ABSTRACT

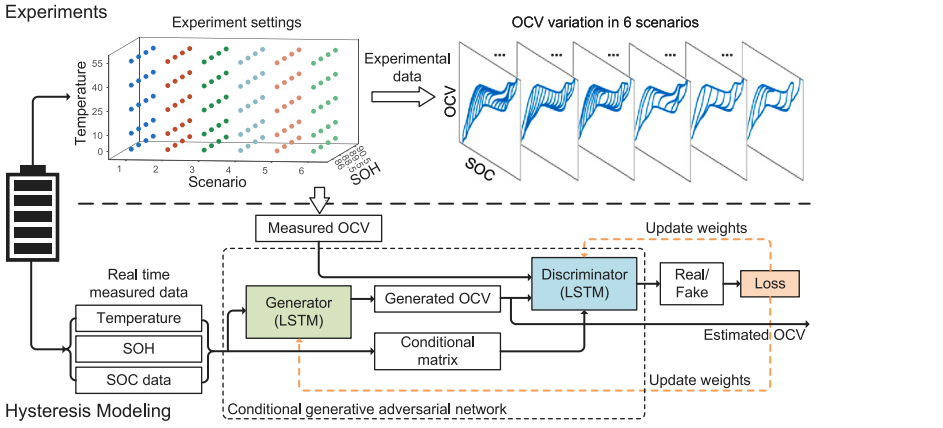

ARTICLE INFO

Keywords:
Lithium iron phosphate (LFP) batteries
Battery modeling
Open circuit voltage
Hysteresis modeling
Data-driven

ABSTRACT

The hysteresis effect represents the difference in open circuit voltage (OCV) between the charge and discharge processes of batteries. An accurate estimation of open circuit voltage considering hysteresis is critical for precise modeling of $LiFePO_4$ batteries. However, the intricate influence of state-of-charge (SOC), temperature, and battery aging have posed significant challenges for hysteresis modeling, which have not been comprehensively considered in existing studies. This paper proposes a data-driven approach with adversarial learning to model hysteresis under diverse conditions, addressing the intricate dependencies on SOC, temperature, and battery aging. First, a comprehensive experimental scheme is designed to collect hysteresis dataset under diverse SOC paths, temperatures and aging states. Second, the proposed data-driven model integrates a conditional generative adversarial network with long short-term memory networks to enhance the model's accuracy and adaptability. The generator and discriminator are designed based on LSTM networks to capture the dependency of hysteresis on historical SOC and conditional information. Third, the conditional matrix, incorporating temperature, health state, and historical paths, is constructed to provide the scenario-specific information for the adversarial network, thereby enhancing the model's adaptability. Experimental results demonstrate that

* Corresponding authors.
E-mail addresses: liheng@csu.edu.cn (H. Li), Weihan.Li@isea.rwth-aachen.de (W. Li).

https://doi.org/10.1016/j.egyai.2025.100478
Received 16 October 2024; Received in revised form 22 December 2024; Accepted 23 January 2025
Available online 31 January 2025

the proposed model achieves a voltage error of less than 3.8 mV across various conditions, with accuracy improvements of 31.3–48.7% compared to three state-of-the-art models.

1. Introduction

Accurate estimation of open circuit voltage (OCV) is crucial for battery modeling and developing an advanced battery management system [1–3]. As the key energy storage components, lithium iron phosphate (LFP) batteries have been widely used in large-scale energy storage and automotive applications due to the advantages of cost-efficiency, exceptional stability, and environmental benignity. However, the hysteresis observed in open-circuit voltage complicates the simple one-to-one SOC-OCV curve, posing a significant challenge for battery modeling and diagnosis [4,5]. Hysteresis manifests as different OCV values for the same SOC level, depending on whether the cell was previously charged or discharged through different paths [6]. It is influenced by many factors, including state-of-charge (SOC), temperature, and battery aging [7–9]. A quantitative characterization of hysteresis and an accurate modeling method is fundamentally important for effective battery management.

Many methods have been proposed for the accurate modeling of open-circuit voltage hysteresis. Generally, these methods can be divided into two categories, analytic-based [10], and data-driven methods. The analytic-based methods establish an analytic formula between SOC and OCV to capture hysteresis [11,12]. For example, in the one-state model, open circuit voltage hysteresis is formulated as a differential relationship with state-of-charge [13,14]. Meanwhile, operator-based methods simulate battery hysteresis as a weighted sum of operators. Based on the different kinds of operators, these methods include the Preisach model [15], Krasnosel'skii–Pokrovskii (KP) model [16], and Prandtl–Ishlinskii (PI) model [17,18]. Subsequently, the hysteresis model can be integrated with equivalent circuit model [19] and advanced Kalman filter [20] for battery state estimation and diagnosis [21]. The analytic-based methods rely on the analytical equations established under specific conditions and thus will be less flexible when applied to varying conditions such as temperature changes and battery degradation [22].

Data-driven methods utilize experimental hysteresis data to establish black-box models for estimating open-circuit voltage through machine learning [23]. Several works have been made using different algorithms, e.g., the forward neural network [24], Gaussian process regression [25] and the recurrent neural network [26,27]. In [24], a compensation module based on a feed-forward neural network is designed to learn the dynamic hysteresis, along with other unmodeled dynamics during charge and discharge transitions. Ko et al. [25] employed a Gaussian process regression model, with partial relaxation voltage data as input, to estimate OCV at charging and discharging. However, the dependency of hysteresis on historical state-of-charge has not been thoroughly explored during modeling.

To mitigate hysteresis influence on open circuit voltage modeling, Xu et al. [26] designed a weighting factor to determine the actual value of open circuit voltage. A long short-term memory network is employed to learn this factor from two major OCV curves during full charge and discharge. However, the hysteresis of minor loops during partial charge and discharge has been neglected. In response, Li et al. [27] developed a long short-term memory network with two hidden layers to specifically capture minor loop hysteresis. However, the influence of temperature and battery degradation has not been fully investigated during modeling, while hysteresis is affected by these two factors significantly [4,8]. Incorporating these factors into modeling is necessary but difficult due to their intertwined influence on hysteresis. Thus, it is necessary to develop a new hysteresis modeling method for LFP batteries by taking these factors into account.

As a new learning paradigm, adversarial learning trains two networks simultaneously in a competitive manner. During the interplay between the generator and discriminator, additional information can be added to condition the model and to enhance the model's robustness and adaptability. In this paper, the adversarial learning is utilized to accurately model the open circuit voltage hysteresis at different temperatures and aging states. Instead of only using the current state-of-charge information, the sequential learning features of the stacked long short-term network are utilized to better capture the dependency of hysteresis on the historical path of state-of-charge to increase modeling accuracy. To enhance the model's adaptability in various situations, two external factors, temperature and battery aging, together with the historical SOC are encompassed as the conditional matrix in a generative adversarial network. The inherent characteristics of hysteresis with these factors can be extracted by using these condition labels during adversarial training process. The experimental hysteresis dataset is obtained by using a very low current rate of C/30 to charge and discharge the batteries under different SOC trajectories. Results demonstrate that the proposed model can generate accurate estimation even under unseen scenarios, and a voltage error of less than 3.8 mV is achieved across diverse conditions. The modeling accuracy increases by 31.3–48.7% compared to three state-of-the-art models, the one-state model, the Prandtl–Ishlinskii model, and a data-driven LSTM model. The contributions of this paper are summarized as follows:

(1) The open circuit voltage hysteresis model is established by using a conditional generative adversarial network integrated with long short-term networks to capture the historical dependency of hysteresis on state-of-charge and improve the estimation accuracy.

(2) Temperature, health state, and historical SOC are constructed as the conditional matrix to provide the scenario-specific information for the network, which increases the adaptability by extracting the dependencies the open circuit voltage hysteresis on various external factors.

(3) A comprehensive experimental scheme is designed to collect hysteresis data for model training and validation. The hysteresis tests involve six scenarios, each conducted at five varying temperatures and four different health states, with each test requiring hundreds of hours.

The organization of this paper is as follows. Section 2 presents the experiment design and hysteresis test procedures. Section 3 elucidates the proposed hysteresis modeling framework, detailing the architecture and training process of the machine learning model. Section 4 presents the results of the hysteresis modeling under various temperatures and aging conditions and compares them with three other state-of-the-art models. Finally, Section 5 concludes the paper and outlines future work.

2. Dataset description

2.1. Experimental setup

To comprehensively investigate hysteresis dependence on battery operating conditions, an experimental scheme was developed and the hysteresis dataset was produced. First, major loop tests were conducted to obtain the OCV curve during full charge and discharge. Minor loop tests were then conducted to capture hysteresis behaviors during partial charge and discharge. To account for temperature and aging effects, the aforementioned tests are repeated at five different temperatures using four cells with varying health states.

The overall experimental sets, as illustrated in Fig. 1, encompass six distinct scenarios involving various hysteresis test cases, five different temperatures, from 0 to 55 °C, and four distinct SOHs, 86%, 88.5%,

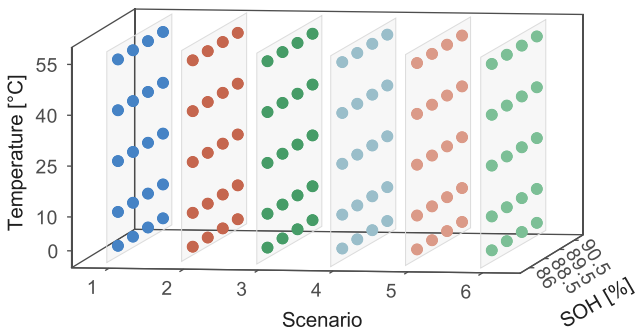

Fig. 1. The experimental set of 4 distinct SOHs, 5 varying temperatures, and 6 different scenarios.

Table 1
Specifics of the tested $LiFeO_4$ battery.

Parameters	Value
Battery type	APR18650m1A
Chemistry	$LiFeO_4$/graphite
Nominal capacity	1100 mAh
Nominal voltage	3.3 V
End of charge voltage	3.6 V
End of discharge voltage	2 V

89.5%, and 90.5%. Each test combination is visually represented by a marker.

These six scenarios are distinguished by the charge/discharge path and SOC interval. Scenario 1: charging hysteresis tests initiated at various SOC levels from 10% to 90% with a 5% increment; Scenario 2: discharging hysteresis test. These tests started at different SOC points from 95% to 20%, also with a 5% interval, capturing hysteresis during discharge; Scenario 3: bidirectional hysteresis test, starting and ending at different SOC levels with a 5% interval; Scenario 4: charging hysteresis test with a wider 10% interval; Scenario 5: discharging hysteresis test with a 10% interval; Scenario 6: bidirectional hysteresis test are repeated but with a 10% SOC interval. Scenarios with denser SOC intervals are represented by darker colors, while lighter colors indicate wider SOC intervals.

The specific experimental setup for hysteresis characterization is shown in Fig. S1, which includes five parts, (1) Thermal chamber: to maintain ambient temperature for the tested cell; (2) Temperature acquisition instrument and thermocouple sensor (PT100): responsible for measuring cell surface temperature and transmitting data to computer; (3) Battery tester. This device controls the charge and discharge process and collects voltage and current data of batteries; (4) Computer, equipped with monitoring software, manages operational settings and logs experimental data; (5) Battery. A specific type of LFP cell, APR18650m1 A, is used in the experiments. The specifications of the tested cell are presented in Table 1.

2.2. Temperature and aging dependency

The impact of temperature on hysteresis behaviors is significant [8]. To quantitatively characterize the temperature dependency, we conducted repetitive hysteresis tests, including major and minor loop tests, at five distinct temperatures, 0, 10, 25, 40, and 55 °C. Fig. 2(a) illustrates the influence of temperature on the major SOC-OCV loops. As temperature rises, the curve transitions from light to dark red. Solid lines represent charging OCV curves, while dashed lines correspond to discharge curves. The hysteresis voltage between charge and discharge curves increases as the temperature drops from 55 °C to 0 °C.

Observations reveal that discharging curves consistently lie below charging curves, with the voltage difference diminishing as the temperature rises. Besides, the temperature fluctuations exert a more

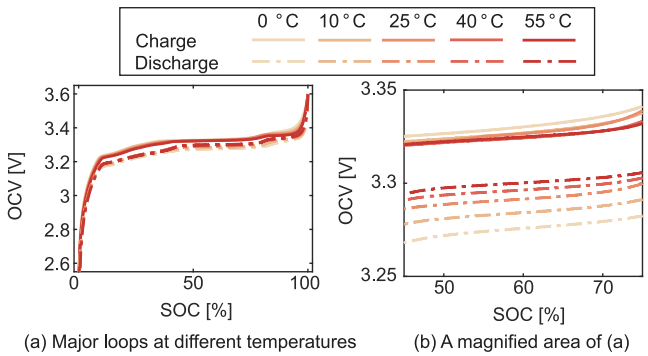

Fig. 2. The fully charged and discharged major loop at different temperatures.

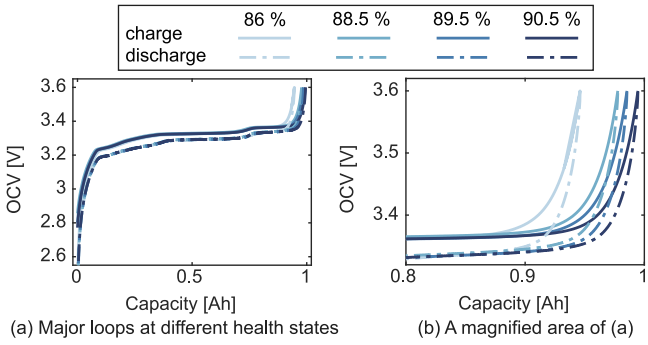

Fig. 3. The fully charged and discharged major loops at different health states.

pronounced effect on discharging curves than on charging curves. The voltage difference between charge and discharge curves can be up to 80 mV at 0 °C. These characteristics have reemphasized the necessity of accurate hysteresis modeling.

Previous studies have demonstrated that aging is another key factor influencing hysteresis [4]. Health state, defined as the ratio of remaining capacity to nominal capacity [28]. The LFP batteries tested in the experiments, with cathode materials of $LiFeO_4$, and graphite anode, have a nominal capacity of 1100 mAh. To determine the remaining capacity of each cell, the constant current and constant voltage (CCCV) protocol is applied to charge the cell, followed by a constant current discharge. The capacity test is repeated 3 times to obtain an average discharge capacity value.

In this study, four cells with different health states of 90.5%, 89.5%, 88.8%, and 86%, respectively, are tested in parallel to capture the hysteresis dependency on aging. Fig. 3(b) compared the OCV curve of cells with different health states. The color of the curves changes from dark blue to light blue as the cell's capacity deteriorates. The OCV curves are shifting to the left during this decrease process.

2.3. Major and minor loop characterization

The major loop test characterizes the OCV curves during the full charge and discharge process. First, the cell undergoes charging from a SOC of 0 to 100% using a small current rate of C/30. Then, the low current method is applied to discharge the cell to SOC = 0%. This sequence yields the major hysteresis loop. Using the low current method, kinetic effects are negligible, and the voltage response is primarily governed by thermodynamic contributions [29]. By applying a current that is small enough, it is assumed that the cell's internal state remains in an equilibrium or quasi-equilibrium state. Thus, the voltage drop caused by internal resistances can be ignored, and the measured voltage can be approximated as the open circuit voltage.

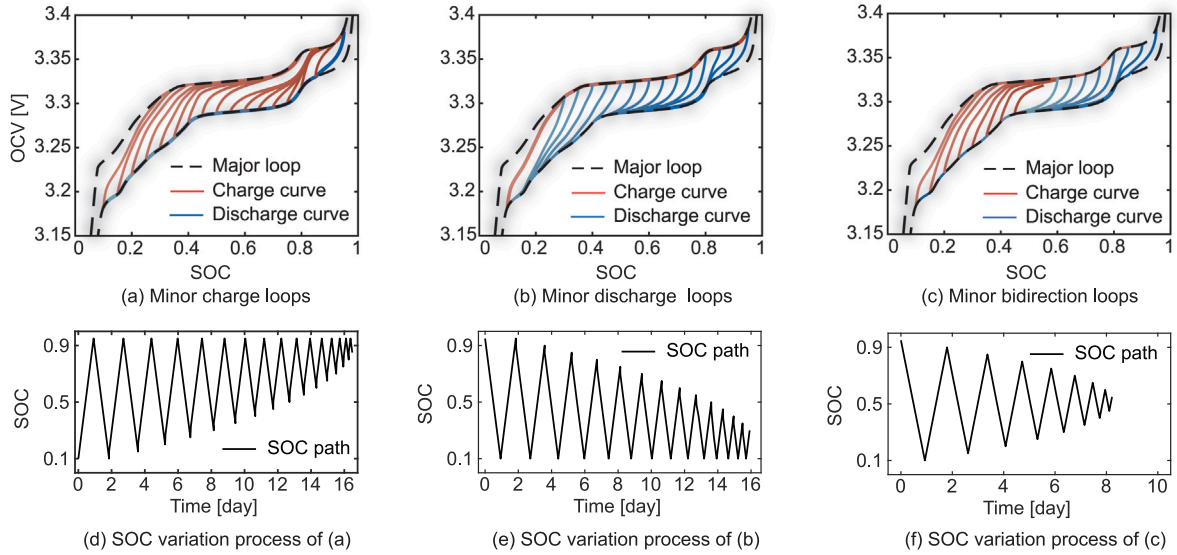

Fig. 4. Charge, discharge, and bidirectional minor loop OCV tests that lie inside between the fully charged and discharged major loop, with their corresponding process of SOC variation. All three minor loop tests are conducted with a current rate of C/30 at 25 °C.

Minor loop tests aim to characterize the minor hysteresis loops at various SOC levels during charge and discharge processes. Three different types of minor loop tests are conducted to comprehensively capture hysteresis during charge, discharge, and simultaneous bidirectional loops.

The purpose of the charging hysteresis test is to characterize hysteresis during battery charging, specifically by varying the SOC starting points while maintaining a consistent ending SOC level. Specifically, the test starts with a cell at SOC = 95%, and the cell undergoes repetitive discharge and charge cycles using a small current (C/30). The sequence begins with discharging the cell from SOC = 95% to 10%. Then the cell is charged back to 95%, followed by another discharge from 95% to 15%. This cyclic process continues until the cell is discharged from 95% to 85%, after which it is charged back to 95%. Fig. 4(a) illustrates the major hysteresis curves represented by gray dashed lines for charge and discharge. Minor loops enclosed by these major curves exhibit hysteresis behavior during the charging process (in red). The discharging process is in blue. Each charging curve originates from a distinct SOC starting point, ranging from 10% to 85%, with a 5% SOC increment. Intuitively, the OCV curve during the discharge period will remain consistent with the major discharge curve. However, the OCV curves during the charging process differ from the major charge curve due to the hysteresis effect. Fig. 4(d) depicts the time-dependent variation of SOC during the charging hysteresis test.

The purpose of the discharge hysteresis test is to characterize voltage hysteresis during battery discharge, specifically by varying the SOC starting points. During this test, the cell is charged from 10% to various SOC levels and discharged to a consistent ending SOC level. Fig. 4(b) illustrates the tests starting at SOC = 10%. First, the cell is charged to 95% and discharged back to 10%. This process continues, varying the SOC starting points from 95% to 30% during discharge. During charging, the OCV curves remain consistent with the major charge curve. However, during discharge, the OCV curves exhibit variations depending on the SOC points. The SOC variation versus time is presented in Fig. 4(e).

A third type of test, the bidirectional hysteresis test, is concentrated to simultaneously capture the hysteresis during both the charge and discharge processes. Initiating with a fully charged cell, it is first discharged to SOC = 95%. After being discharged with C/30 to SOC = 10%, the cell is charged back to 90%. This cycle continues, decrementing the SOC by 5% during each charge and discharge process. Finally, the cell is discharged from SOC = 60% to 45% and then charged to 55%. Fig. 4(c) displays the SOC-OCV curves obtained from the bidirectional test, where the charging curves are depicted in red, while the discharge curves are shown in blue. The SOC variation of the aforementioned charge and discharge process is plotted in Fig. 4(f). For convenience, the datasets from these three scenarios are referred to as dense datasets as the SOC increment between each loop is 5%. Conversely, scenarios 4–6 are termed sparse datasets, given the SOC gap is 10%.

The aforementioned hysteresis test datasets can be used for model training and validation. To capture hysteresis accurately, and to enhance the model's adaptability under various conditions, a data-driven OCV hysteresis model which integrates conditional generative adversarial network and long short memory networks is introduced in the next section.

3. Data-driven hysteresis modeling

3.1. The proposed modeling framework

Conceptually, hysteresis is characterized by the system's responsiveness to its input history [5]. In OCV hysteresis modeling, it is essential to consider the temporal dependencies and nonlinearities between the historical SOC and the current OCV [30]. Besides, factors including temperature and aging state must be considered during modeling due to their impact on hysteresis behavior.

Machine learning methods are adept at depicting nonlinear relationships. Among these, LSTM networks were specifically designed for sequence learning, which excels in learning from historical information and handling complex long-term dependencies. Therefore, it is reasonable to consider using LSTM to capture this intricate relationship inherent in battery hysteretic behaviors.

To further enhance the model's adaptability under different scenarios, e.g., different temperatures, and aging states, a conditional generative adversarial network (CGAN) is incorporated with the LSTM networks to integrate the aforementioned conditional information into the adversarial learning process. This allows the model to capture the intricate dependencies of hysteresis on external factors while leveraging the sequential learning capabilities of LSTM networks. Unlike traditional GANs, CGANs can generate scenario-specific outputs, making them particularly suitable for modeling hysteresis under diverse operating conditions. Besides, the model can remain accurate even under

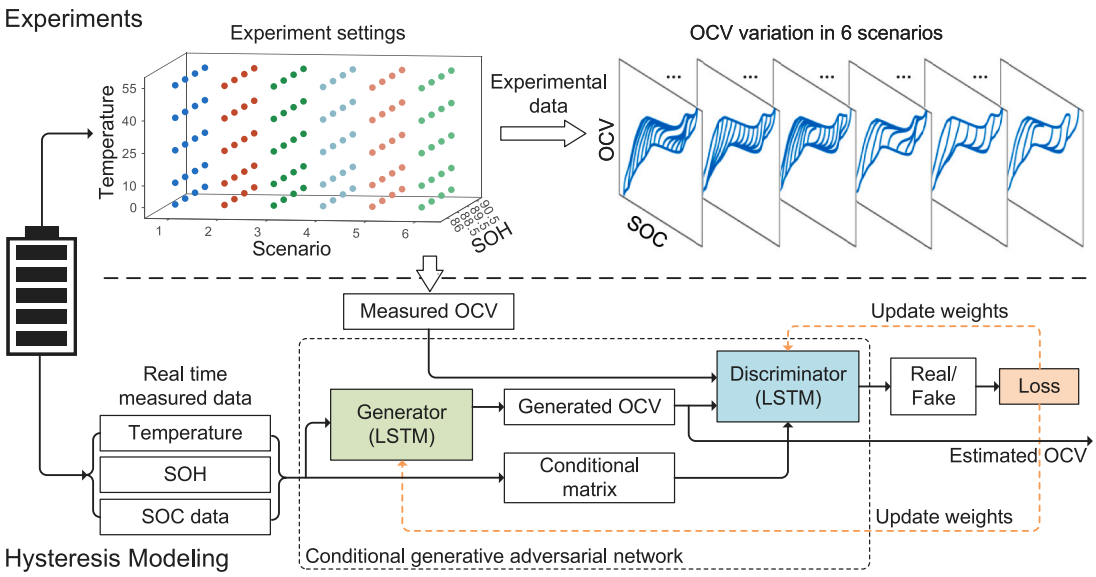

Fig. 5. The proposed conditional generative adversarial networks for OCV hysteresis modeling.

unseen conditions owing to the dynamic adaptability of adversarial learning.

Fig. 5 provides an overview of the proposed data-driven modeling method for OCV hysteresis, which is divided into two major parts, experimental data collection and hysteresis modeling. The hysteresis data are collected across six distinct scenarios, five varying temperatures, and four SOHs. After preprocessing, the experimental data of each parameter combination are prepared for subsequent modeling. To achieve accurate and robust hysteresis modeling, the proposed method integrates a conditional generative adversarial network with long short-term memory (LSTM) networks to capture the historical dependencies of hysteresis. The conditional matrix, incorporating battery state information, are utilized to enhance the model's adaptability by providing scenario-specific information during adversarial training.

Specifically, both the generator and discriminator are designed based on the LSTM networks. Temperature, the health state of batteries, and the historical SOC are provided as scenario-specific information to construct the conditional matrix, which is then used as input for the generator to estimate the open circuit voltage. The discriminator outputs a probability to determine whether a sample is from measurement or generation. The estimation accuracy is improved through the continuous adversarial learning process. To conserve testing resources and enhance modeling efficiency, data collected from sparse loops (scenario 4–6 with a 10% SOC interval) are utilized to train the network. The model is then tested on denser loop datasets (scenario 1–3 with a 5% SOC interval), which include scenarios not encountered during training. The model demonstrates robust interpolation and extrapolation capabilities across diverse operating conditions.

3.2. Conditional generative adversarial network

A conditional generative adversarial network (CGAN), as an improvement in the basic GAN architecture, can associate the generated data with conditional information. This network is composed of two major parts, a generator G and a discriminator D. The former generates new plausible samples similar to the original data, aiming to deceive the discriminator, the main task of which is to determine whether a sample is from measurements or generation. The generator and discriminator continue to evolve until they reach a Nash equilibrium [31]. The training process is finished when the discriminator cannot tell the difference between the real data and the generated data.

For the discriminator, D, it is expected to have a higher probability of $D(\boldsymbol{x})$ for the real samples $\boldsymbol{x}$ while a lower probability of $D(G(z))$ for the generated sample $G(z)$. Thus, the loss function can be formulated as follows,

$$L_D = -\mathbb{E}_{\boldsymbol{x}\sim P(\boldsymbol{x})}[\log D(\boldsymbol{x})] - \mathbb{E}_{z\sim P(z)}[\log(1 - D(G(z)))] \tag{1}$$

where $\boldsymbol{x}$ represents the real data samples that include the historical SOC sequence s and battery external factors, ambient temperature T and battery health state Q. z represents random noise input, which is used to generate synthetic OCV samples by the generator G. $P(x)$ and $P(z)$ are the distribution of the real data samples and noise input z, respectively. $\mathbb{E}$ denotes expectation.

For the generator, G, the goal is to maximize the probability $D(G(z))$ for the generated sample.

$$L_G = \mathbb{E}_{z\sim P(z)}[\log(1 - D(G(z)))] \tag{2}$$

For the conditional generative adversarial network architecture, the objective function $L(D,G)$ is formulated to balance the adversarial training process between the generator G and the discriminator D. The objective function is defined as follows:

$$\min_G \max_D L(D,G) = \mathbb{E}_{x\sim P(x)}[\log D(x|q)] + \mathbb{E}_{z\sim P(z)}[\log(1 - D(G(z|q)))] \tag{3}$$

where q represents the conditional information. In this model, temperature, health state, and historical SOC path are selected as inputs for extra information, which helps the model capture the features under various conditions. Both the generator and discriminator comprise a stacked LSTM network, where the output of the former is the estimated OCV value and the discriminator outputs a probability of the real sample.

3.3. Long short-term memory network

LSTM networks were specifically designed for sequence learning, which excels in learning from historical information and handling complex long-term dependencies. Therefore, it is reasonable to consider using LSTM to capture this intricate relationship inherent in battery hysteretic behaviors. The special memory units enable the network to learn long-term dependencies in sequential data. Each memory cell is equipped with an internal state, represented by C, and many multiplicative gates, including the input gate I, the forget gate F, and the output gate O that control the flow of information.

In this study, a stacked 3-layer LSTM is established to capture the complex dependency of hysteresis in battery open circuit voltage. A

fully connected layer is appended to the LSTM layer for the output at time step t. The model input is a vector comprising three parameters denoted as $\boldsymbol{x}_t = [s_t, T, Q]$. s_t is the historical SOC path up the current time step t. T represent the temperature and Q denotes the health state of the battery. Both temperature T and capacity Q are normalized using the equations as follows,

$$T = \frac{T_{cell}}{T_{max} - T_{min}} \tag{4}$$

$$Q = \frac{Q_{cell} - 0.8 * Q_{nom}}{(1 - 0.8) * Q_{nom}} \tag{5}$$

where T_{cell} is the surface temperature of the cell, and T_{max} and T_{min} are the maximum and minimum operating temperatures of the cell respectively. In this work, T_{max} is 60 °Cand T_{min} is −30 °C. For battery state of health, Q_{cell} represents the current capacity of the cell, and Q_{nom} is the battery nominal capacity. The health state Q is normalized to a value between 0 and 1, reflecting the battery's condition relative to its nominal capacity. Specifically, when the SOH drops to 80% of its nominal value, the battery is considered to have reached the limit of its first service life. This normalization ensures that both temperature and health state are scaled appropriately for input into the LSTM network.

The input $\boldsymbol{x_t}$ and the hidden state H_{t-1} of the previous time step are fed into the LSTM gates. The LSTM gates include the input gate I_t, the forget gate F_t, and the output gate O_t, as shown in Eqs. (6)–(8). These gates are computed using fully connected layers with sigmoid activation functions (σ), which map the input values to the interval $(0, 1)$. The equations for these gates are as follows:

$$I_t = \sigma(W_i \times \boldsymbol{x_t} + U_i \times H_{t-1} + b_i) \tag{6}$$

$$F_t = \sigma(W_f \times \boldsymbol{x_t} + U_f \times H_{t-1} + b_f) \tag{7}$$

$$O_t = \sigma(W_o \times \boldsymbol{x_t} + U_o \times H_{t-1} + b_o) \tag{8}$$

$$\tilde{C}_t = \tanh(W_g \cdot \boldsymbol{x_t} + U_g \times H_{t-1} + b_g) \tag{9}$$

$$C_t = F_t \odot C_{t-1} + I_t \odot \tilde{C}_t \tag{10}$$

$$H_t = O_t \times \tanh(C_t) \tag{11}$$

Additionally, the input node $\tilde{C}_t$ is introduced to compute the candidate cell state. This node uses a tanh activation function, which maps the input to the interval $(-1, 1)$. The cell state C_t is updated based on the aforementioned gates, which can store specific information that the LSTM processes continuously, enabling the long-term memory mechanism. Finally, the hidden state H_t is calculated by a point-wise multiplication between the output gate O_t and the cell state C_t with a tanh operation.

The LSTM network is designed to capture the long-term dependencies in the historical SOC path, while also incorporating the influence of temperature and health state. This enables the model to accurately estimate the open circuit voltage with hysteresis, even under varying operating conditions.

3.4. Model training and evaluation

The hyperparameters employed during the training process are outlined in Table 2. The LSTM network is configured with an input size of 3, a hidden size of 128, a stack size of 3, and an output size of 1. The training epoch number is set as 2000 to ensure sufficient training to capture the complex dependencies in the data. A batch size of 32, and a learning rate of 0.001 is chosen to balance convergence speed and stability. During each epoch, the mean square error between the ground truth and simulated values is chosen as the loss function. The 'Adam' optimizer is utilized to compute and update the model parameters, minimizing the fitting error. To avoid the overfitting problem during network training, early termination of the training process is adopted if the model's performance on the test set deteriorates.

Table 2
Hyperparameters of the LSTM network and training settings.

	Criteria	Value
Model parameters	Input size	3
	Hidden size	128
	Output size	1
	Stack size	3
Training settings	Epoch	2000
	Batch size	16
	Learning rate	0.001
	Optimizer	Adam
	Loss function	Mean square error

The proposed networks were implemented on Python 3.9 with PyTorch 2.1.1. All experiments ran on a laptop with an i7-12700H CPU, 16 GB random access memory and an RTX 3050 GPU with 4 GB memory. The computation time for the training and testing processes to evaluate the efficiency of the proposed model. The training process, which involved 2000 epochs, required a total of 50.23 min. The testing process, conducted on the charge hysteresis dataset with over 4800 samples, took 0.17 s of computation time. Once the model is trained, the relatively low computation time for testing indicates that it could be deployed in real-time applications with minimal latency.

Three evaluation matrices, the mean relative error (MRE), mean square error (MSE), and root mean square error (RMSE), are calculated between the estimated and measured OCV for evaluating the model's performance. The formulas for these matrices are presented below,

$$\text{MRE} = \frac{1}{n}\sum_{k=1}^{n}\left|(\hat{y}_k - y_k)/y_k\right| \tag{12}$$

$$\text{MSE} = \frac{1}{n}\sum_{k=1}^{n}\left(\hat{y}_k - y_k\right)^2 \tag{13}$$

$$\text{RMSE} = \sqrt{\frac{1}{n}\sum_{k=1}^{n}\left(\hat{y}_k - y_k\right)^2} \tag{14}$$

$$\text{Accuracy} = \left(1 - \frac{\left|\hat{y}_k - y_k\right|}{V_{hys}^{MAX}}\right) \times 100\% \tag{15}$$

where $\hat{y}_k$ represents the estimated voltage of the hysteresis model at k time step, and y_k is the measured voltage. n represents the length of the voltage sequence. V_{hys}^{MAX} in Eq. (15) represents the maximal voltage difference between the charge and discharge major curve.

4. Results and discussion

4.1. Model evaluation under different temperatures

First, the proposed model was tested under different temperatures on an individual cell. The hysteresis dataset is partitioned into a sparse loop part (with a 10% SOC gap, i.e., scenarios 4–6) and a dense loop part (with a 5% SOC gap, i.e., scenarios 1–3). The model is trained using sparse loop data collected at three temperatures: 0 °C, 25 °C, 55 °C. Then, the dense loop data at these three temperatures is utilized to evaluate the model's estimation accuracy at different SOC levels. Last, the dense loop data at 10 °C and 40 °C is assigned to a second test set to verify the model's ability to interpolate to unseen test conditions.

The estimation results of the interpolation model at five temperatures in scenario 6 are illustrated in Fig. 6. Subfigure (a)–(e) depicts the comparison between the measured voltage (represented by a black line) and the estimated voltage (shown as a blue dashed line). It can be seen that the model trained on sparse loop data can accurately capture

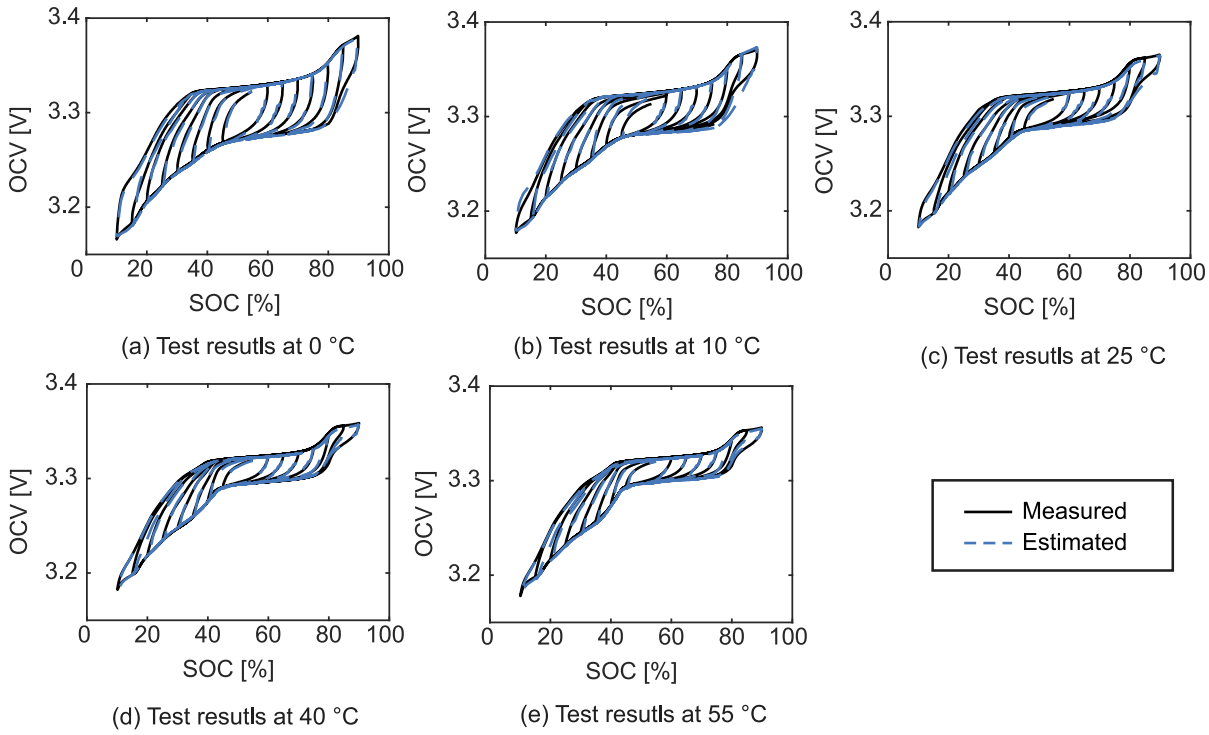

Fig. 6. The modeling results of open circuit voltage hysteresis under five different temperatures.

Table 3
The evaluation of the proposed model under five different temperatures.

Temperature	Scenario	Interpolation			Extrapolation		
		MRE ($\times 10^{-4}$)	MSE	RMSE (mV)	MRE ($\times 10^{-4}$)	MSE	RMSE (mV)
0 °C	1	4.335	5.141	2.267	11.91	33.98	5.829
	2	5.704	6.325	2.515	11.14	26.31	5.129
	3	4.753	5.858	2.420	9.451	19.43	4.409
10 °C	1	7.560	12.83	3.582	5.207	6.172	2.484
	2	5.819	9.458	3.075	3.909	2.926	1.711
	3	5.576	8.557	2.925	4.596	4.298	2.073
25 °C	1	5.307	6.327	2.515	4.883	5.285	2.299
	2	5.853	4.980	2.232	4.230	2.927	1.711
	3	5.846	5.859	2.421	4.439	3.300	1.817
40 °C	1	4.404	4.346	2.085	4.036	2.420	1.556
	2	3.102	2.139	1.463	3.976	2.442	1.563
	3	3.711	3.429	1.852	4.287	2.797	1.672
55 °C	1	4.380	4.136	2.034	5.294	5.572	2.361
	2	4.627	3.166	1.779	5.393	5.086	2.255
	3	4.737	5.207	2.282	4.767	5.116	2.262

the hysteresis behaviors, even on the test set of dense loop data. As the temperature decreases from 55 °C to 0 °C, the measured hysteresis becomes more pronounced. This phenomenon arises because the hysteresis voltage between charge and discharge major loops is larger at lower temperatures. Besides, the minor loop hysteresis gradually approaches two major hysteresis curves during charge or discharge.

To further validate the model's ability to extrapolate across different temperatures, first, the sparse loop data collected at 10 °C, 25 °C, 40 °C is utilized to train the model. Then the dense loop data at 0 °C and 55 °C is employed to test the model's ability to extrapolate to different conditions as these two temperatures are beyond the measuring range of the training set. The error between estimated and measured voltage under each scenario and temperature is calculated to evaluate modeling accuracy. Fig. 7 shows the distribution of accuracy at each test condition in the form of split violin charts. The dashed line in the middle of each density plot shows the ends of the first and third quartiles of the error sequence, with a black line in the center representing the median error.

Fig. 7 illustrates the modeling accuracy across five different temperatures and three scenarios. In each test condition, the left half of the violin plot corresponds to the performance of the "interpolation" model, while the right side represents the results from the "extrapolation" model. The quantitative modeling results are detailed in Table 3. It can be seen that the RMSE of the interpolation model remains below 2.6 mV at 0 °C, 25 °C, and 55 °C. The model demonstrates satisfactory results when interpolated to 40 °C, whereas an average RMSE of 3.2 mV is observed during testing the model at 10 °C. The pronounced variation in hysteresis at lower temperatures likely contributes to this phenomenon.

The RMSE of the "extrapolation" model can be reduced to 1.6 mV at 40 °C, while the error remains below 2.5 mV at 10 °C, 25 °C, and 40 °C. When extrapolating the model to 0 and 55 °C, the average RMSE is 5.12 and 2.29 mV, respectively. Comparing the performance of interpolation and extrapolation at 0 °C, it is obvious that the model achieves better results when interpolating. This could be attributed to that interpolation occurs within the range of observed data, which

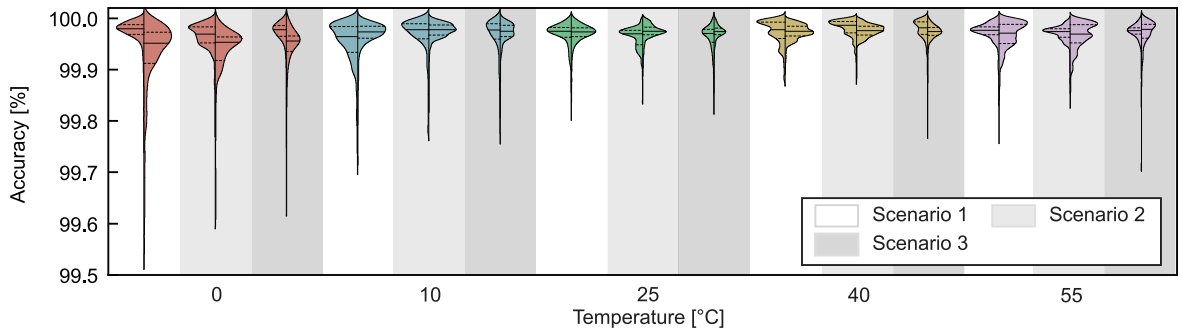

Fig. 7. The accuracy distribution of the OCV estimation results of the proposed model under different temperatures and scenarios.

Table 4
The evaluation of the proposed model on four cells with different SOHs.

Cell No.	Scenario	MRE ($\times 10^{-4}$)	MSE	RMSE (mV)
Cell 1 (SOH = 86%)	1	7.125	14.38	3.793
	2	5.510	6.654	2.579
	3	5.091	6.738	2.595
Cell 2 (SOH = 88.5%)	1	3.964	4.114	2.028
	2	2.906	1.836	1.355
	3	3.335	2.773	1.665
Cell 3 (SOH = 89.5%)	1	5.979	6.508	2.551
	2	5.097	5.035	2.244
	3	5.248	5.489	2.342
Cell 4 (SOH = 90.5%)	1	7.914	11.86	3.444
	2	6.804	7.828	2.798
	3	7.705	10.31	3.211

enables the model to have more information to make an accurate estimation.

4.2. Model evaluation under different SOHs

To further verify its generalization ability to battery aging, the model is tested on cells with different SOHs. Four cells with ascending SOHs from 86% to 90.5% are tested in this study. The dataset from three batteries is selected as the training set, and the model is tested on the 4th cell. For example, sparse loop data under 0 °C, 25 °C, 55 °C from cell 1–3 are used to train the model. Then, the model is tested on the dense loop data of cell 4 at 10 and 40 °C. The modeling results on four cells at 40 °C are presented in Table 4.

The model consistently performs well across various cells. Specifically, it achieves an average RMSE of 1.68 mV for cell 2 and 2.38 mV for cell 3 in three scenarios. In contrast, the average RMSE for cell 1 and 4 is 2.99 mV and 3.15 mV, respectively. Notably, the average RMSE for cell 2 and 3 is lower than those for cell 1 and 4. This difference could be due to the model's training process: interpolation occurs during training on cell 1, 3, 4, and testing on cell 2, while extrapolation occurs during testing on cells 1 and 4.

It can also be noted that the model's performance may slightly degrade as the battery ages, but it remains robust within the tested SOH range. Future work will focus on further validating the model's long-term performance and exploring strategies to mitigate any potential degradation in accuracy over extended periods of use.

4.3. Comparison with other hysteresis models

The proposed hysteresis model is rigorously evaluated against three prominent state-of-the-art models, namely, the Plett single state model [10], the Prandtl–Ishlinskii model [32], and another machine learning model [27]. The PSS model formulates hysteresis as a differential relationship with battery SOC, serving as a benchmark of physics-based hysteresis model due to its simplicity and interpretability. The PI model, as another prominent physics-based model, simulates hysteresis using operators, which is often used in applications where hysteresis needs to be captured with high accuracy. The LSTM model serves as a representative data-driven model for comparison with the proposed approach. This comparison aims to demonstrate the superiority of the proposed method in accuracy, generalization, and adaptability to diverse operating conditions. These three models are parameterized with the same dataset used to train the proposed model. The specific structure and parameterization methods for the PSS and PI models are detailed in the supplementary materials.

The modeling results of four different methods in three scenarios at 25 °C are shown in Fig. 8. The measured voltage is shown as a black line, while the other four modeling methods are represented by lines with different colors and types. Fig. 8(a) illustrates the estimated OCV of different models on a segment of scenario 1, with a magnified view of the interval between 400 and 500 min. Fig. 8(b) illustrates the simulated voltage of the three models versus the measured voltage. The black line, with a slope equal to 1 represents the actual voltage. The red represents the ML model, the blue symbolizes the PSS model and the green corresponds to the PI model. The closer these points are to the black line, the more accurate the result. Fig. 8(c) demonstrates the probability of modeling error occurring within each interval. We extend our analysis to scenario 2 and 3. Fig. 8(d) ~ (f) presents the test result of these three models on scenario 2, while Fig. 8(g) ~ (f) compares these models on scenario 3. Notably, the error distribution of the proposed model mainly lies within the range of [−3 3] mV, which is more accurate than the other three. Detailed quantitative evaluation metrics are summarized in Table 5.

The quantitative evaluations of these four models are summarized in Table 5. The proposed model achieves an average RMSE of 2.39 mV in three scenarios, while the RMSE of the other three models: the LSTM model (3.48 mV), the PSS model (4.66 mV), and the Prandtl–Ishlinskii model (4.47 mV). The modeling error of the proposed model is decreased by 31.3%, 48.7%, and 46.5% compared with the LSTM model, the PSS model, and the PI model.

The proposed model's ability to handle both temperature and SOH variations highlights its strength as a data-driven approach. Unlike the

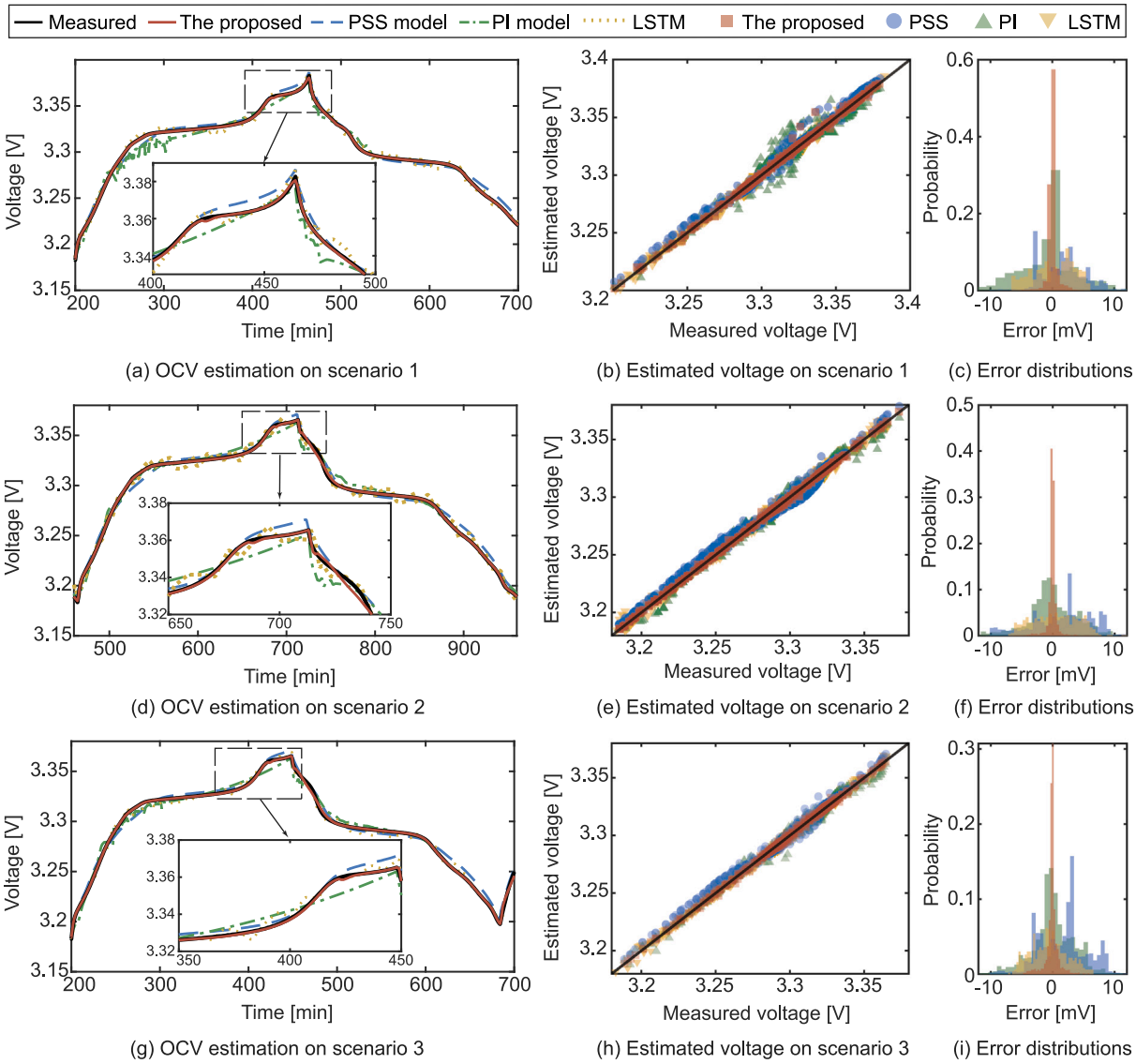

Fig. 8. Comparisons of the OCV estimation and error distributions of different methods in three scenarios. (a)~(c) demonstrate the modeling results on scenario 1; (d)~(f) depict the comparisons on scenario 2, and (g)~(i) illustrate the modeling results for all four models on scenario 3.

Table 5
The evaluation of the proposed model with three other modeling methods.

Model	Scenario	MRE ($\times 10^{-4}$)	MSE	RMSE (mV)
The proposed model	1	5.307	6.327	2.515
	2	5.853	4.980	2.232
	3	5.846	5.859	2.421
LSTM [27]	1	8.534	10.747	3.278
	2	8.776	11.941	3.455
	3	9.453	13.732	3.706
PSS [14]	1	10.59	20.75	4.555
	2	13.27	26.45	5.143
	3	10.66	18.21	4.267
PI [18]	1	11.80	36.82	6.068
	2	8.827	15.43	3.929
	3	7.523	11.61	3.407

other two physics-based models, which often require reparameterization for different operating conditions, the proposed model leverages machine learning techniques to learn the complex dependencies of hysteresis directly from data. This makes it more versatile and adaptable to real-world scenarios. Additionally, the adversarial training process in CGAN allows the model to refine its estimates iteratively, leading to higher accuracy in capturing the nuances of hysteresis behavior. In contrast, the PSS model, being a differential-based approach, struggles

with the nonlinear and path-dependent nature of hysteresis, while the PI model, although more flexible, still relies on predefined operators that may not fully capture the complexity of the data.

5. Conclusions

Establishing an accurate relationship between open circuit voltage and the state of charge is crucial for precise battery modeling. In this paper, a novel data-driven approach is proposed to accurately model open circuit voltage hysteresis in $LiFePO_4$ batteries, considering the complex dependencies on state-of-charge, temperature, and battery aging. A comprehensive experimental scheme was designed to quantify hysteresis under diverse conditions, providing a robust dataset for model training and validation. An accurate and robust hysteresis model combining conditional generative adversarial networks and long short-term memory networks is proposed to capture the historical dependencies and enhancing adaptability through conditional information. The most significant advantage of the proposed model over existing hysteresis models lies in its robust adaptability across different temperatures and aging conditions. By incorporating these factors as conditional information in the adversarial training process, the proposed model maintains its accuracy even when deployed under different operating conditions. The modeling results demonstrate an RMSE of 2.37 mV during interpolation and 2.61 mV during extrapolation across different temperatures. The comparative analysis demonstrates that the proposed model achieves an average RMSE of 2.39 mV in three test scenarios under 25 °C, which is decreased by 31.3%, 48.7%, and 46.5% compared with the LSTM model, the PSS model, and the PI model, respectively. Future work will focus on integrating the proposed hysteresis model with an equivalent circuit models or electrochemical models to further enhance its performance in real-world applications.

CRediT authorship contribution statement

Lisen Yan: Writing – original draft, Visualization, Validation, Software, Methodology, Investigation, Conceptualization. **Jun Peng:** Writing – review & editing, Supervision, Funding acquisition. **Zeyu Zhu:** Writing – review & editing, Investigation, Data curation. **Heng Li:** Writing – review & editing, Supervision, Methodology, Funding acquisition. **Zhiwu Huang:** Writing – review & editing, Supervision. **Dirk Uwe Sauer:** Writing – review & editing, Supervision. **Weihan Li:** Writing – review & editing, Supervision, Methodology, Funding acquisition.

Declaration of competing interest

The authors declare that they have no known competing financial interests or personal relationships that could have appeared to influence the work reported in this paper.

Acknowledgments

This work is partially supported by the Natural Science Foundation of China (No. 52377221, 62172448), and the Natural Science Foundation of Hunan Province, China (No. 2023JJ30698). Part of the work is supported by the research project "COBALT-P" (16BZF314C), funded by the German Federal Ministry for Economic Affairs and Climate Action (BMWK). Lisen Yan is supported by China Scholarship Council (Grant No. 202206370146).

Appendix A. Supplementary data

Supplementary material related to this article can be found online at https://doi.org/10.1016/j.egyai.2025.100478.

Data availability

Data will be made available on request.

References

[1] Pang Y, Dong A, Wang Y, Niu Z. Deep learning from three-dimensional lithium-ion battery multiphysics model part ii: Convolutional neural network and long short-term memory integration. Energy AI 2024;17:100398.
[2] Hofmann T, Hamar J, Mager B, Erhard S, Schmidt JP. Transfer learning from synthetic data for open-circuit voltage curve reconstruction and state of health estimation of lithium-ion batteries from partial charging segments. Energy AI 2024;100382.
[3] Zhao J, Qu X, Wu Y, Fowler M, Burke AF. Artificial intelligence-driven real-world battery diagnostics. Energy AI 2024;18:100419.
[4] Van der Ven A, See KA, Pilon L. Hysteresis in electrochemical systems. Batter Energy 2022;1(2):20210017.
[5] Röder F, Ramasubramanian S. A review and perspective on path dependency in batteries. Energy Technol 2022;10(11):2200627.
[6] Ovejas V, Cuadras A. Effects of cycling on lithium-ion battery hysteresis and overvoltage. Sci Rep 2019;9(1):1–9.
[7] Ruan H, Chen J, Ai W, Wu B. Generalised diagnostic framework for rapid battery degradation quantification with deep learning. Energy AI 2022;9:100158.
[8] Marongiu A, Nußbaum FGW, Waag W, Garmendia M, Sauer DU. Comprehensive study of the influence of aging on the hysteresis behavior of a lithium iron phosphate cathode-based lithium ion battery–an experimental investigation of the hysteresis. Appl Energy 2016;171:629–45.
[9] Li F, Liu R, Liu J, Li H. Voltage hysteresis in transition metal oxide cathodes for li/na-ion batteries. Adv Funct Mater 2023;2300602.
[10] Plett GL. Extended kalman filtering for battery management systems of lipb-based hev battery packs: Part 2. modeling and identification. J Power Sources 2004;134(2):262–76.
[11] Kwak M, Lkhagvasuren B, Park J, You J-H. Parameter identification and soc estimation of a battery under the hysteresis effect. IEEE Trans Ind Electron 2019;67(11):9758–67.
[12] Wycisk D, Oldenburger M, Stoye MG, Mrkonjic T, Latz A. Modified plett-model for modeling voltage hysteresis in lithium-ion cells. J Energy Storage 2022;52:105016.
[13] Roselyn JP, Ravi A, Devaraj D, Venkatesan R. Optimal soc estimation considering hysteresis effect for effective battery management in shipboard batteries. IEEE J Emerg Sel Top Power Electron 2020;9(5):5533–41.
[14] Gao Y, Plett GL, Fan G, Zhang X. Enhanced state-of-charge estimation of lifepo4 batteries using an augmented physics-based model. J Power Sources 2022;544:231889.
[15] Li Z, Shan J, Gabbert U. A direct inverse model for hysteresis compensation. IEEE Trans Ind Electron 2020;68(5):4173–81.
[16] Chayratsami P, Plett GL. Hysteresis modeling of lithium–silicon half cells using prandtl–ishlinskii model. In: 2020 IEEE 16th international conference on control & automation. IEEE; 2020, p. 1578–83.
[17] Al Janaideh M, Xu R, Tan X. Adaptive estimation of play radii for a prandtl–ishlinskii hysteresis operator. IEEE Trans Control Syst Technol 2021;29(6):2687–95.
[18] He Y, He R, Guo B, Zhang Z, Yang S, Liu X, et al. Modeling of dynamic hysteresis characters for the lithium-ion battery. J Electrochem Soc 2020;167(9):090532.
[19] Wang S, Zhang S, Wen S, Fernandez C. An accurate state-of-charge estimation of lithium-ion batteries based on improved particle swarm optimization-adaptive square root cubature kalman filter. J Power Sources 2024;624:235594.
[20] Wang S, Takyi-Aninakwa P, Jin S, Yu C, Fernandez C, Stroe D-I. An improved feedforward-long short-term memory modeling method for the whole-life-cycle state of charge prediction of lithium-ion batteries considering current–voltage-temperature variation. Energy 2022;254:124224.
[21] Wang S, Fan Y, Jin S, Takyi-Aninakwa P, Fernandez C. Improved anti-noise adaptive long short-term memory neural network modeling for the robust remaining useful life prediction of lithium-ion batteries. Reliab Eng Syst Saf 2023;230:108920.
[22] Wu Y, Huang Z, Li D, Li H, Peng J, Stroe D, et al. Optimal battery thermal management for electric vehicles with battery degradation minimization. Appl Energy 2024;353:122090.
[23] Wu B, Widanage WD, Yang S, Liu X. Battery digital twins: Perspectives on the fusion of models, data and artificial intelligence for smart battery management systems. Energy AI 2020;1:100016.
[24] Pozzato G, Li X, Lee D, Ko J, Onori S. Accelerating the transition to cobalt-free batteries: a hybrid model for lifepo4/graphite chemistry. Npj Comput Mater 2024;10(1):14.
[25] Ko C-J, Chen K-C. Using tens of seconds of relaxation voltage to estimate open circuit voltage and state of health of lithium ion batteries. Appl Energy 2024;357:122488.

[26] Xu Z, Wang J, Fan Q, Lund PD, Hong J. Improving the state of charge estimation of reused lithium-ion batteries by abating hysteresis using machine learning technique. J Energy Storage 2020;32:101678.
[27] Li F, Zhang S, Li H, Xia Y, Yan L, Huang Z. Exploring the hysteresis effect of li-ion batteries: A machine learning based approach. In: 2023 International joint conference on neural networks. IEEE; 2023, p. 1–8.
[28] Yan L, Peng J, Gao D, Wu Y, Liu Y, Li H, et al. A hybrid method with cascaded structure for early-stage remaining useful life prediction of lithium-ion battery. Energy 2022;243:123038.
[29] Ovejas V, Cuadras A. State of charge dependency of the overvoltage generated in commercial li-ion cells. J Power Sources 2019;418:176–85.
[30] Barcellona S, Colnago S, Piegari L. Aging effect on lithium-ion battery resistance hysteresis. IEEE Trans Ind Appl 2023.
[31] Huang B, Salgia S, Zhao Q. Disagreement-based active learning in online settings. IEEE Trans Signal Process 2022;70:1947–58.
[32] Al Janaideh M, Al Saaideh M, Tan X. The prandtl–ishlinskii hysteresis model: Fundamentals of the model and its inverse compensator [lecture notes]. IEEE Control Syst Mag 2023;43(2):66–84.